JGR Planets

RESEARCH ARTICLE
10.1029/2024JE008773

Key Points:

- Groundwater sapping processes in Hack crater on Mars led to crater infilling, lake formation, valley incision and deposition of fans
- The groundwater level is determined by the morphology of erosional features and is consistent with estimates from geophysical models
- Depositional features permit reconstruction of the putative water volumes contained within the formed lake

Supporting Information:

Supporting Information may be found in the online version of this article.

Correspondence to:

A.-C. Plesa,
Ana.Plesa@dlr.de

Citation:

De Toffoli, B., Plesa, A.-C., Luzzi, E., & Hauber, E. (2025). Groundwater sapping in Hack crater (Mars): Geologic evidence and geophysical modeling of groundwater stability. *Journal of Geophysical Research: Planets*, *130*, e2024JE008773. https://doi.org/10.1029/2024JE008773

Received 28 SEP 2024
Accepted 5 MAY 2025

Author Contributions:

Conceptualization: B. De Toffoli, A.-C. Plesa, E. Luzzi, E. Hauber
Data curation: B. De Toffoli, A.-C. Plesa, E. Luzzi
Formal analysis: B. De Toffoli, A.-C. Plesa
Investigation: B. De Toffoli, A.-C. Plesa, E. Hauber
Methodology: B. De Toffoli, A.-C. Plesa, E. Luzzi
Software: A.-C. Plesa, E. Luzzi
Visualization: B. De Toffoli, A.-C. Plesa, E. Luzzi
Writing – original draft: B. De Toffoli, A.-C. Plesa, E. Luzzi, E. Hauber

Groundwater Sapping in Hack Crater (Mars): Geologic Evidence and Geophysical Modeling of Groundwater Stability

B. De Toffoli[1,2], A.-C. Plesa[2], E. Luzzi[3], and E. Hauber[2]

[1]Department of Geosciences, University of Padova, Padova, Italy, [2]Institute of Space Research, DLR, Berlin, Germany, [3]School of Engineering, Mississippi Mineral Resources Institute, The University of Mississippi, University, MS, USA

Abstract This study investigates Hack crater in Arabia Terra on Mars, which exhibits remarkable water-related landforms, suggesting a period of intense water activity despite lacking a connection with large-scale fluvial networks. Instead, short valleys within its walls display morphologies indicative of mass-wasting processes driven by groundwater seepage. These valley heads located at approximately −2,900 m provide insights into the groundwater table during landform development, and suggest sustained groundwater supply after the crater's formation at 3.5 Ga. For the first time, we combine geological analyses and geophysical models to investigate the depth of groundwater at this location using two independent approaches. By analyzing the locations and the topography of water-related features, we identify key events that shaped the area, from the appearance of a closed lake due to groundwater influx to its eventual disappearance. After crater excavation, groundwater influx from subsurface sources started driven by sapping processes, filled the basin, and created valleys and depositional features. The system likely persisted until groundwater reservoir exhaustion or until top-down freezing of the groundwater conduits into the crater. The basin dry-out led to the exposure of water-related morphologies to subaerial erosion. Our study provides insights into the multi-stage evolution of a Martian lake formed through groundwater sapping, offering an alternative hypothesis to surface runoff-dominated scenarios. Despite possible regional implications due to the basin's water levels matching the hypothesized global shoreline levels, caution is warranted in extrapolating these findings on a planetary scale, as surrounding craters do not exhibit comparable water-related features indicating a possibly localized phenomenon.

Plain Language Summary The analysis of morphological features inside a Martian crater suggests significant water activity despite the absence of connections to large-scale river systems. Short valleys within the crater walls, displaying characteristics indicative of erosion and sediment transportation driven by groundwater seepage, contribute to the understanding of these phenomena. As supported by our observations and modeling, after the crater formation, groundwater started leaking into the impact depression, filling the basin and forming valleys and deposition features. The system likely persisted until exhaustion of the groundwater reservoir or until top-down freezing of the groundwater conduits into the crater. The basin dry-out exposed water-related features to erosion. The maximum elevations of these valleys, approximately −2,900 m, provide insights into the groundwater table depth during the formation of these landforms, pointing to a sustained groundwater supply post-crater formation about 3.5 billion years ago. This study offers crucial insights into the evolution of a Martian lake, highlighting the role of groundwater sapping in contrast to scenarios involving surface runoff. While the basin's water levels align with the global shoreline, caution is suggested in extrapolating these findings planet-wide. Neighboring craters lack similar water-related features, suggesting a possible localized phenomenon.

1. Introduction

Arabia Terra, located at the transition between the northern lowlands and southern highlands on Mars, hosts a variety of landforms associated with a past of pervasive aqueous processes. This is suggested by multiple lines of evidence, including spectral signatures of hydrated minerals (Di Pietro et al., 2023; Mège et al., 2023; Milliken et al., 2005; Poulet et al., 2005; Schmidt et al., 2022; Zabrusky et al., 2012), light-toned layered sedimentary deposits interpreted to indicate aqueous depositional processes (Pondrelli et al., 2015, 2019), sapping valleys (Salese et al., 2019), paleolakes (Dickeson et al., 2022), inverted fluvial channels (Davis et al., 2016;

Mirino, 2022; Zaki et al., 2021), and terrestrial analogs for groundwater upwelling (Schmidt et al., 2023). Because Arabia Terra lies on a broad circular albedo feature, previous studies proposed that such feature would mark an ancient impact crater, or alternatively was formed by paleotectonic processes, and that the region was subsequently enriched in water throughout the Noachian, originating from a regional aquifer (Dohm et al., 2007). The hydrological activity within this regional aquifer was later investigated by Andrews-Hanna et al. (2010), who modeled the groundwater activity through the Noachian and early Hesperian and found a possible scenario where initially the hydrological activity is predicted to be confined locally within individual craters. After these depressions had been filled with sediments, the continuous rise of the groundwater table would have spread the playa environments laterally to the intercrater plains (Andrews-Hanna et al., 2010).

Although the scientific community reached a broad consensus in interpreting Arabia Terra as a region with a past prevalence of aqueous processes in the Early Noachian, the climatic conditions in place during such hydrological activity are still debated. Wordsworth et al. (2013) presented their "icy highlands" model, where the melting of ice sheets located at high elevations would feed the valley networks without a prolonged water input, but rather in an ephemeral setting. In this regard, Davis et al. (2016) argue that the volumes of water required to produce the observed fluvial landforms are not consistent with ephemeral activity, but instead extensive precipitation and runoff in a warm and wet climate seem more plausible. This conclusion has been recently supported by Dickeson et al. (2022), whose geomorphological observations suggest that the climate was warm enough to allow fluvial and lacustrine processes to be protracted throughout the Noachian. Moreover, evidence of prolonged fluvial activity during the Noachian was also presented by Salese et al. (2020) in the NW Hellas Basin, where the conditions necessary to produce the observed morphologies must have been characterized by a hydrological cycle governed by rainfall. Later, at the Noachian-Hesperian boundary, the climatic conditions would have shifted from warmer and wetter to arid, as attested by the mineralogical change from phyllosilicates to evaporites (Zabrusky et al., 2012) and other mineralogic evidence. Nevertheless, a warm period characterized by abundant atmospheric precipitations was proposed to have occurred in the Late Hesperian in the cratered highlands (Craddock & Howard, 2002), in the equatorial region of Valles Marineris (Mangold et al., 2004), in paleolakes distributed globally (Cabrol & Grin, 2001; Goudge et al., 2015), and in Gale crater (Palucis et al., 2016). Such warm and wet periods might have been intermittent (Palucis et al., 2016), although evidence for sustained flow with the formation of highly branched valley networks and other fluvial landforms was also reported, suggesting a prolonged stability (e.g., Mangold et al., 2004; Salese et al., 2020). Therefore, the climatic shift toward cold and dry conditions might have been more gradual than anticipated, allowing surface water to be at least intermittently stable throughout the Hesperian epoch.

In this work, we examine the Hack impact crater roughly centered at 27.8°N and 11.5°E in the northeastern portion of Arabia Terra (Figure 1a). It is characterized by the presence of multiple fan-shaped deposits on its floor (Figure 4; De Toffoli et al., 2021; Irwin et al., 2005; Ori, Marinangeli, & Baliva, 2000; Ori, Marinangeli, & Komatsu, 2000; Salese et al., 2019), exhibiting an impressive preservation of water-related features (Figures 1b and 2a). Depositional features can be identified as fan deltas when they appear as fan-shaped deposits fed by a channel, characterized by a flat top and a single steep scarp or by a stack of steep scarps of decreasing radius (De Villiers et al., 2009, 2013; Gilbert, 1885; Hauber et al., 2009). These traits help to visually distinguish, in imagery and topographic data sets, deltas from alluvial fans that appear instead as gently sloping semi-conical landforms which transition smoothly toward the flat crater floor. Deltas are also associated with the discharge of water and sediments from a confined channel into a basin filled with water. Alluvial fans form in subaerial environments and thus differ from deltas by not being related to standing bodies of water (e.g., Moore & Howard, 2005; Morgan et al., 2014, 2022). As noted by Irwin et al. (2005), this crater has the deepest crater floor elevation over a wide surrounding area, which indicates that the deposits on the crater floor may be related to a hypothetical regional groundwater table at an elevation of ∼−4,000 m, which was also suggested by the global study performed by Salese et al. (2019).

For the first time, we conducted comprehensive geomorphological analyses and mapping of this crater, equipped with models highlighting thermal conditions at the time of crater formation, presenting a new geomorphic map of the area and providing a detailed inventory of water-related features and their topographic characteristics beyond just fan-shaped deposits. We confirm and expand upon earlier interpretations (De Toffoli et al., 2021; Irwin et al., 2005; Ori, Marinangeli, & Baliva, 2000; Ori, Marinangeli, & Komatsu, 2000; Salese et al., 2019), which provided a more general view of this area, with a novel multidisciplinary perspective integrating geological information with geophysical models, enabling a more robust analysis. This study provides evidence for

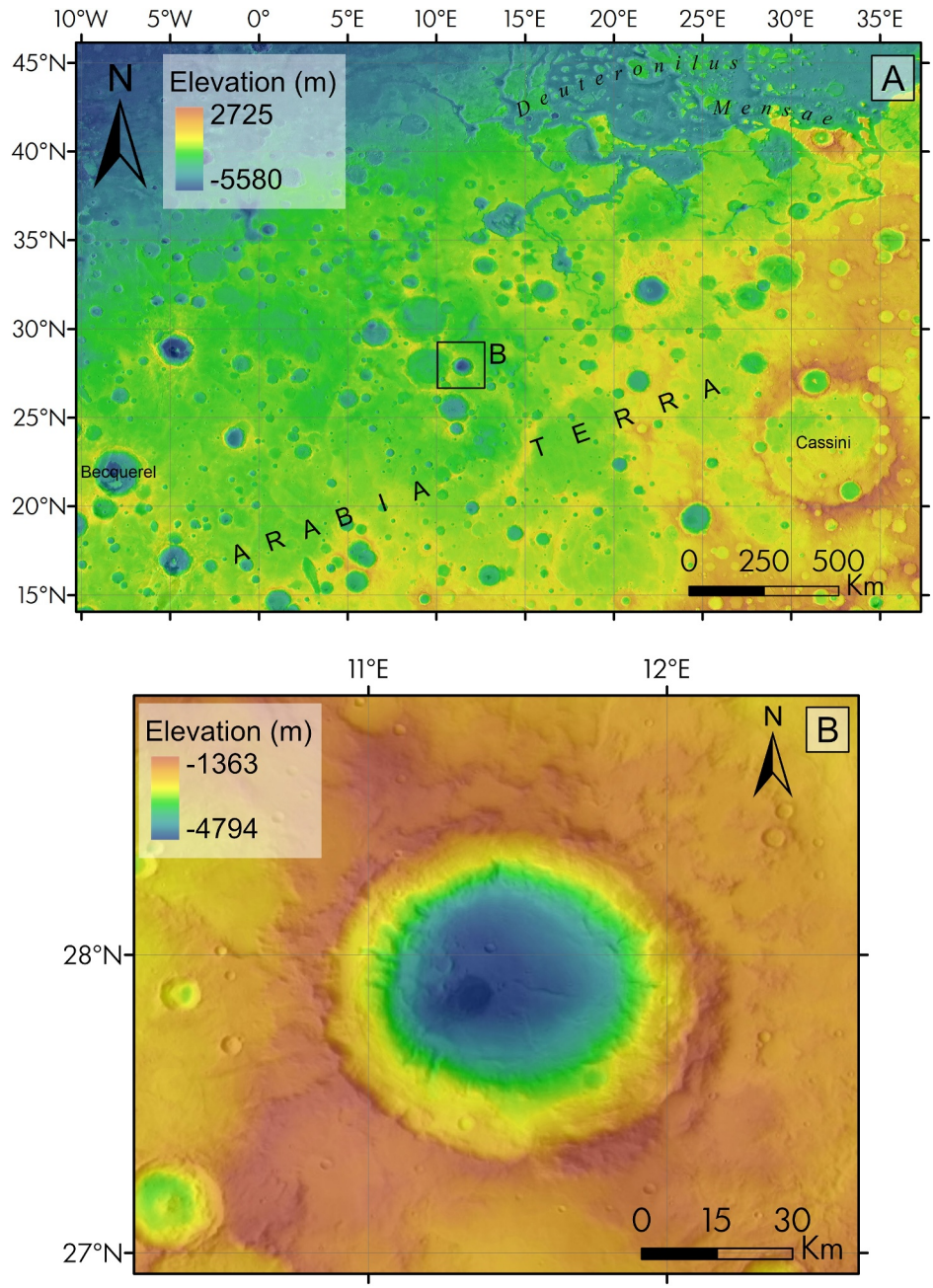

Figure 1. Location and topography of the study crater. (a) Regional context (MOLA-HRSC blended Digital Elevation Model (DEM) overlying in semi-transparency the Viking Global mosaic). The study area is highlighted in the black box and displayed in close-up view in panel (b) that shows the MOLA-HRSC blended DEM (Fergason et al., 2018) overlying in semi-transparency the CTX mosaic processed and made available by the Murray Lab (Dickson et al., 2023).

groundwater sapping in a Martian crater and enables reconstructing the sequence of events within this region, providing valuable insights into the amount of water required to form the observed landforms, which is directly relevant for understanding the past climate and associated geological processes. In this context, we calculated the volumes of water filling the crater at two distinct times—first, when the water level corresponded to the delta fronts, and second, when the water level corresponded to the valley tips, where the channels transitioned to delta morphology. Furthermore, we modeled the groundwater depth at the time of crater formation. The results of these numerical models help evaluate whether the observed landforms are consistent with the thermal conditions necessary for groundwater to exist at this location. Our findings provide a first necessary step for further analyses

probing the interaction between impact processes and groundwater sapping, significantly contributing to the current understanding of the Martian hydrogeological evolution.

2. Materials and Methods

2.1. Geomorphological Observations

For our geomorphological observations, we relied on imagery from the Context Camera (CTX; ∼6 m/pixel) global mosaic (Dickson et al., 2018; Malin et al., 2007), imagery from the High Resolution Imaging Science Experiment (HiRISE; 25–50 cm/pixel) (McEwen et al., 2007), and the nighttime infrared mosaic from the Thermal Emission Imaging System (THEMIS; ∼100 m/pixel) (Christensen et al., 2004). For a regional topographic context, we used the Mars Orbiter Laser Altimeter (MOLA) elevation model (∼460 m/pixel; Smith et al., 2001; Zuber et al., 1992). Observations, mapping, and measurements were made using the QGIS software, and for age determination we determined the size-frequency distributions (CSFD) of impact craters (Hartmann & Neukum, 2001). To produce the geomorphic map, we used the plugin Mappy for QGIS (https://plugins.qgis.org/plugins/mappy/). We mapped at a 1:350,000 scale, following the standards recommended by the United States Geological Survey (USGS) and the Federal Geographic Data Committee (FGDC) for planetary mapping (FGDC, 2006). Craters with a diameter larger than 1 km were mapped, while smaller craters were not considered suitable for the chosen output scale of 1:1,200,000.

2.2. Volumetric Estimations

The CTX Digital Elevation Models (DEMs) used in this work were downloaded as raw images from the PDS Geosciences Node (http://ode.rsl.wustl.edu/). The IDs of the images used are listed in Table 1. Image processing was carried out using the USGS Integrated Software for Imagers and Spectrometers (ISIS3; Becker et al., 2007). After radiometric corrections, calibration, and georeferencing, the stereo pairs were processed through the Ames Stereo Pipeline (ASP; Beyer et al., 2018), where the stereo algorithm was run. The resulting point clouds were then aligned to the MOLA global topography to improve accuracy, and they were finally converted to DEMs.

Volumetric estimations were carried out using the 3D point cloud and mesh processing CloudCompare (CC) software (cloudcompare.org; Penasa et al., 2021). In the CC environment, through the 2.5D Volume Calculation Tool, it is possible to estimate volumes between a point cloud and an arbitrary plane, thus efficiently simulating the given case scenario of water volumes inside an impact crater.

2.3. Thermal Modeling

We used global thermal evolution models (Plesa et al., 2016, 2018, 2022) to estimate the potential groundwater depth that we define as the depth at which the temperature is high enough to allow for the presence of pure liquid water in the Martian subsurface (see discussion on the presence of salts in Section 4.1). To this end, we assume that ice is present in the subsurface at this location and by comparing the local subsurface temperature with the melting temperature of water ice we calculate the depth at which ice would melt and become liquid water. Our models employ the most recent constraints on the interior structure of Mars from InSight (Interior Exploration using Seismic Investigations, Geodesy and Heat Transport) seismic data (Knapmeyer-Endrun et al., 2021; Stähler et al., 2021). The crustal thickness in our models is obtained from the joint inversion of gravity and topography data and anchored by seismic measurements at the InSight landing site (Wieczorek et al., 2022). The geodynamic model includes the crustal thickness variations, with a thick crust beneath volcanic areas and a thin crust below impact basins (Figure 2), by assigning a lower thermal conductivity and higher concentrations of heat producing elements to the crustal regions. For a detailed description of the coupling between the geodynamic and crustal thickness models, we refer the reader to Plesa et al. (2016), while further details about the crustal thickness models are discussed in Wieczorek et al. (2022). We note that our models do not explicitly include a topography (i.e., the topography is only considered indirectly through the crustal thickness variations). Thus, the surface is located at the same level everywhere, a global average 0-level (Figure 2). This allows us to directly compare our model results of groundwater depth with the geological analyses that estimate the depth of groundwater features relative to the global 0-level MOLA elevation. In Figure 2, we illustrate our approach of comparing the groundwater depth obtained from the local estimates based on the geological analyses and the 3D global thermal evolution models. We note that the term "ground water depth" used throughout this paper is equivalent to the elevation potential or elevation head in this study.

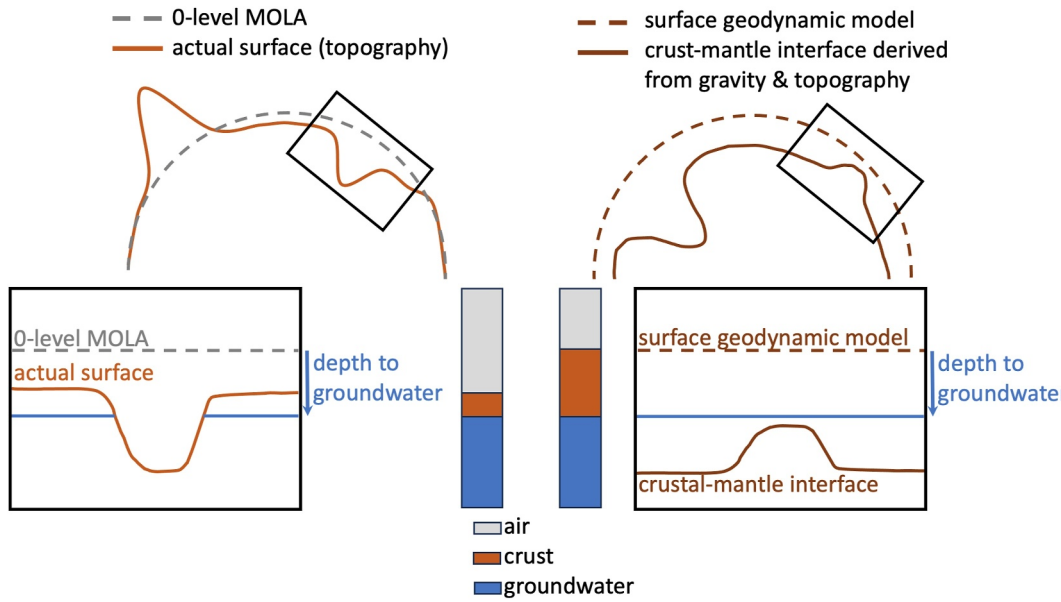

Figure 2. Sketch illustrating the comparison between the groundwater depth derived from geological analyses (left) and geodynamical thermal evolution models (right). While the geological analyses are related to the local topography, the geodynamic models have a flat surface, but implicitly include the topography signal through the crustal thickness that is based on the joint inversion of gravity and topography data.

We used several crustal thickness models that were presented by Wieczorek et al. (2022) to test the effects of crustal thickness variations on the depth of groundwater. The thermal conductivity of the crust has a first-order effect on the subsurface thermal state and hence on the depth of groundwater. A low crustal thermal conductivity and/or a thick crust increase(s) the insulating effect of the crust, which acts as a blanket on the mantle and lithosphere. This leads to warmer subsurface temperatures and a shallower groundwater depth. In our models, we use constant crustal thermal conductivity values of 2 and 3 W/(mK) (Clauser & Huenges, 1995; Seipold, 1998), and test models with a temperature- and porosity-dependent thermal conductivity (Clifford et al., 2010). Additional parameters related to the crustal models tested here are available in Supporting Information S1 and in Wieczorek et al. (2022).

Our models consider latitudinal variations of the mean annual surface temperature (Kieffer, 2013; Ohring & Mariano, 1968) with values of −57°C on average, increasing from −128°C at the poles to −38°C at the equator, and showing a value of −49°C at the crater location. In addition to the thermal conductivity, the surface temperature is one of the most important parameters controlling the thermal state of the near-surface layers and hence the depth of groundwater. A detailed discussion of the consequences of the surface temperature and other model parameters for the groundwater depth can be found in Section 4.

3. Results

3.1. Geomorphological Observations, Mapping, and Age Determination

We focused our attention on Hack crater of around 70 km diameter located in the northeastern portion of Arabia Terra. According to global geological mapping, it lies on Amazonian and Hesperian Impact units (AHi) (Tanaka et al., 2014). The global map published by Tanaka et al. (2014) does not resolve small-scale features that are only detectable on high resolution imagery. The geomorphological observations carried out in our work led to the

Table 1
IDs of the CTX Images Processed Into Digital Elevation Models for This Work

Stereo Pair #1	B16_015918_2080_XN_28N348W	F20_043438_2080_XI_28N348W
Stereo Pair #2	J18_051930_2081_XI_28N348W	F10_039746_2074_XI_27N348W

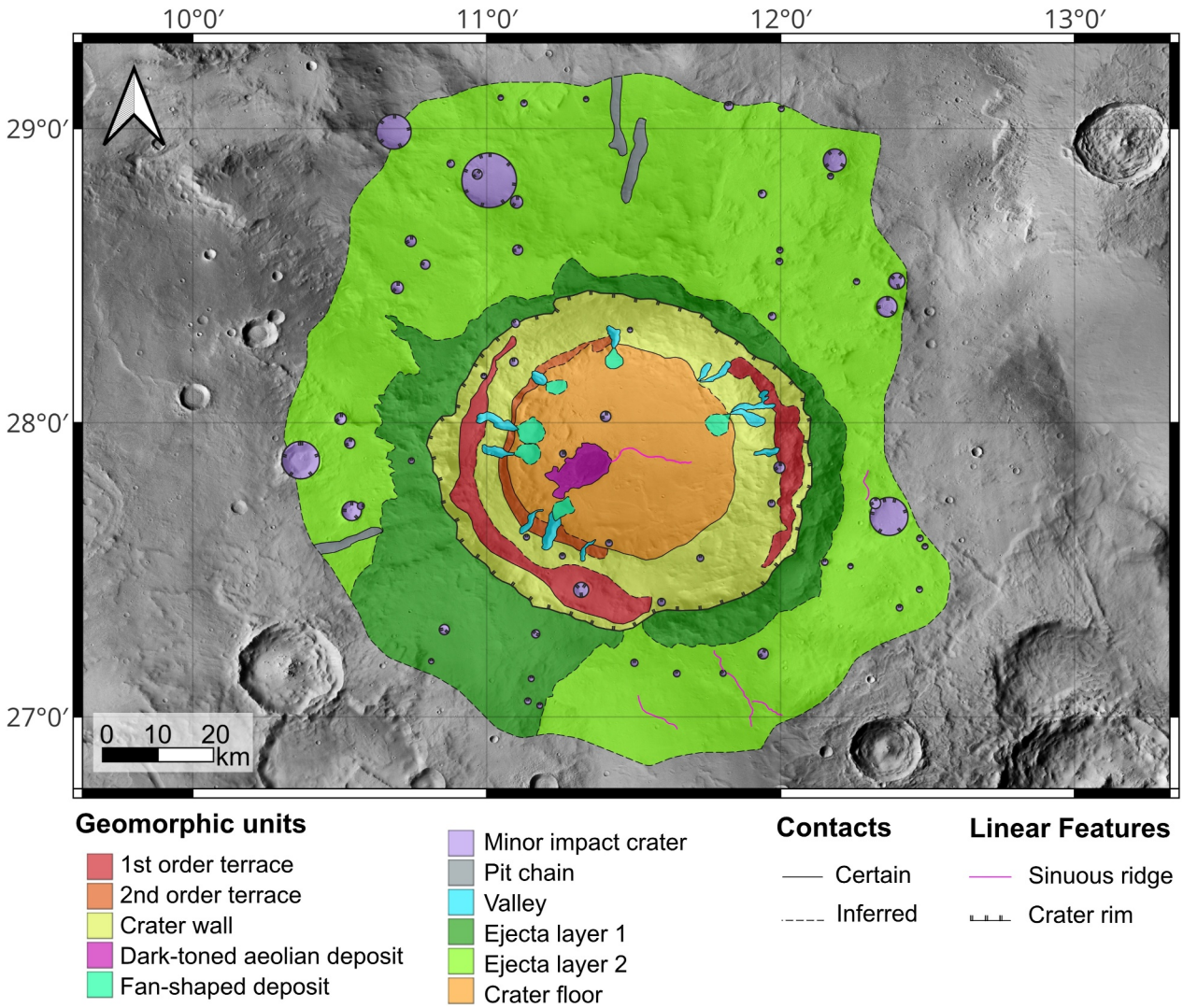

Figure 3. Geomorphic map at a 1:1,200,000 scale (top) and associated legend (bottom). Basemap: CTX mosaic by MurrayLab (Dickson et al., 2018).

production of a geomorphic map at a 1:1,200,000 scale, where features larger than 1 km in diameter/length are resolved (Figure 3). The scale chosen for our geomorphic map did not allow us to map gullies, but we report their widespread presence and we show an example in Figure 4a.

We observed and mapped 12 valleys on the crater walls and six fan-shaped stepped deposits on the crater floor (Figure 4b). While both the valleys and the fan-shaped deposits are generally well preserved, in some instances the fan-shaped deposits are partially covered by dust and were therefore mapped as an inferred contact. In addition to the valleys and fan-shaped deposits, we mapped two different terrace levels, although their continued expression throughout the crater is often eroded/overprinted or covered by dust, and therefore was mapped as an inferred contact. The terraces were particularly well visible on the western side of the crater, which overall appears more pristine and less degraded compared to the eastern part. One terrace appears to have an elevation between approximately −3,500 and −3,750 m, at around the same elevation of the valley tips, while the other stands well above between about −2,300 and −2,500 m. It is well established that terraces can form through impacts into a layered substrate, which includes icy or water-abundant layers that alter the subsurface rheology (e.g., Bramson et al., 2015). In the examined crater, the lower terrace corresponds to the elevation of the valley tips, while the higher terrace falls close to the valley heads, highlighting a good match between terraces and water-related landforms observed on the crater walls.

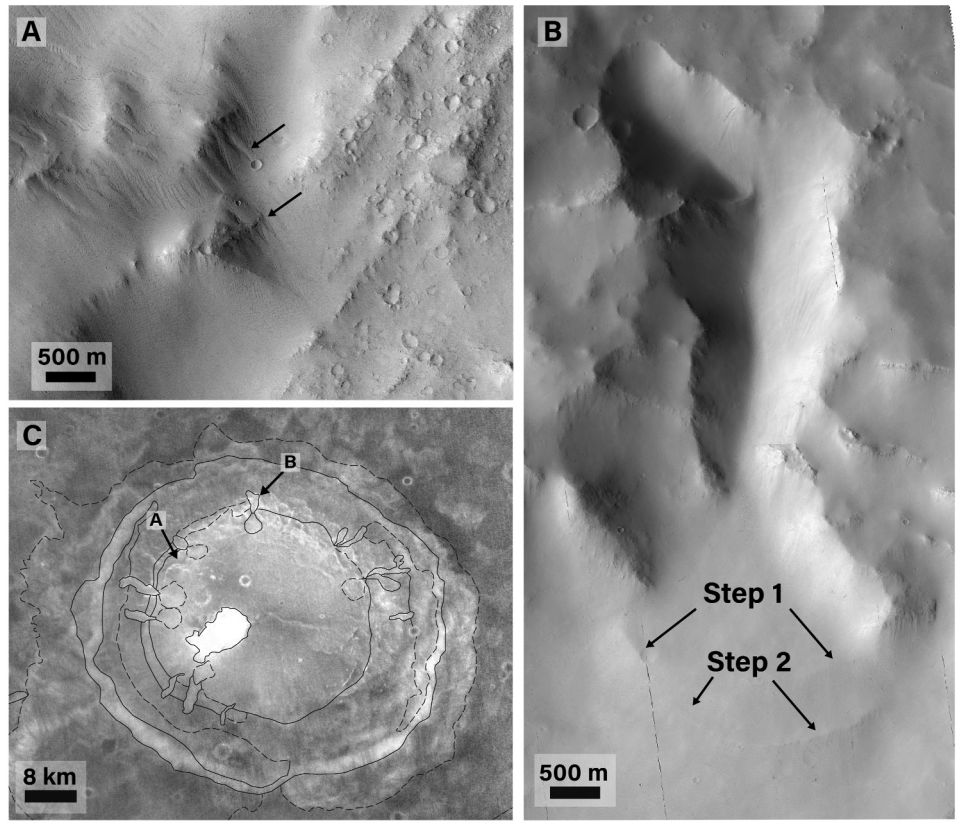

Figure 4. (a) Multiple gullies (black arrows) occurring on the NW portion of the crater wall. HiRISE image ESP_016696_2085. (b) Valley and stepped delta in the N portion of the crater. Two different steps of the delta are indicated by black arrows. HiRISE image ESP_016485_2085. (c) THEMIS nighttime infrared mosaic underlying the contacts of the geomorphic units reported in Figure 3. Note the high thermal inertia of the dark-toned deposit located roughly at the crater floor center. The locations of panels (a and b) are indicated by black arrows.

A dark-toned aeolian deposit occurs roughly at the center of the crater floor, and is not observed elsewhere. The nighttime infrared data set shows the dark-toned deposit exhibiting high thermal inertia (Figure 4c). Such high thermal inertia suggests that it is composed of materials that can absorb and retain heat efficiently, such as dense volcanic rocks or highly indurated/cemented/compacted sediments. Although we cannot entirely rule out a volcanic origin without spectral analyses, we lean toward an interpretation involving aqueous alteration, diagenesis, or cementation, since aqueous erosion and deposition are observed throughout the crater, providing the elements needed for these processes to occur. Furthermore, the dark appearance of this deposit resembles more a surficial halo rather than a well-defined volcanic deposit.

The ejecta consists of at least two layers, one external and one closer to the crater rim. The contact between the two ejecta layers is not always unequivocal. In the southwestern part of the map, a tonal difference is clearly noticeable, with the ejecta closer to the crater rim appearing lighter. However, this difference becomes more subtle in the northeastern part of the map, where we only relied on topographic variations. Consequently, the contact between the two ejecta layers was also mapped as an inferred contact. Two large pit chains were mapped in the northern part of the external ejecta (ejecta layer 2).

Isolated sinuous ridges occur both within the crater floor and outside the crater on the intercrater plain. The sinuous ridge located at the center of the crater floor exhibits high thermal inertia in the nighttime infrared mosaic (Figure 4c). Thus, these ridges may also represent indurated/cemented deposits that resisted aeolian erosion better than the surrounding materials. Nevertheless, we cannot exclude that their origin might be related to tectonic or impact-induced deformational processes, similar to the wrinkle ridges commonly observed on Mars.

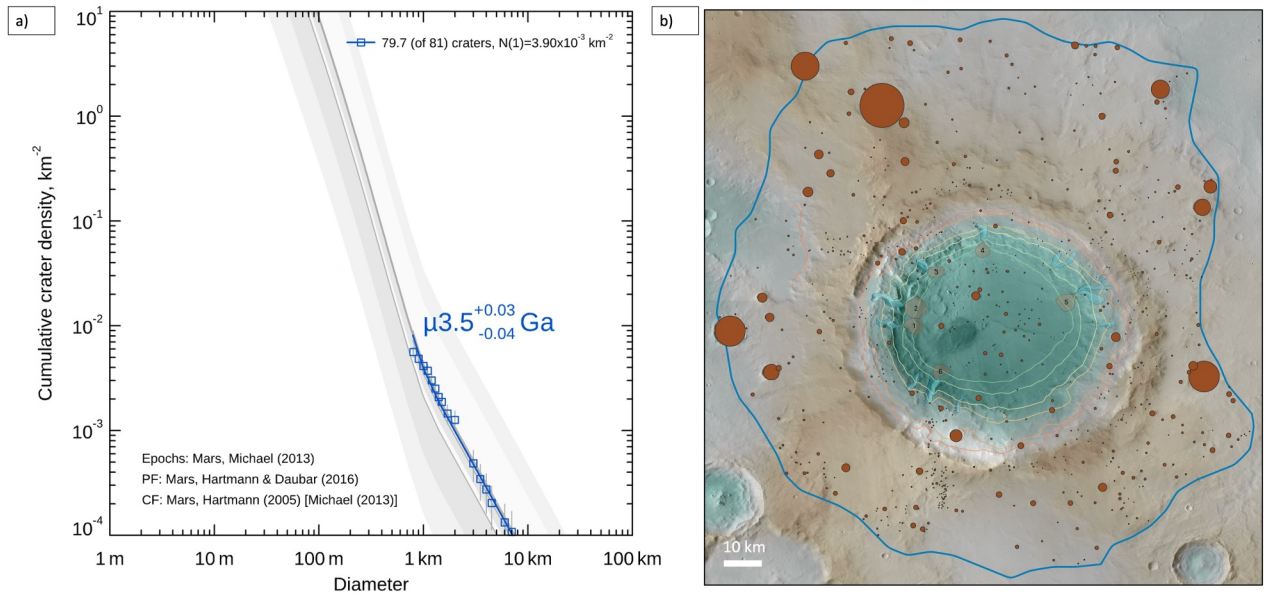

Figure 5. (a) CSFD (crater size-frequency distributions) model age estimate for the whole crater area included within the ejecta limit, as shown in panel (b), which illustrates a CTX mosaic overlain by false color elevation from Mars Orbiter Laser Altimeter.

We further constrained the crater absolute model age to a higher degree of detail through CTX-derived impact crater statistics (chronology functions: Hartmann & Neukum, 2001; Michael, 2013; production function: Ivanov et al., 2001), obtaining an impact age of 3.5 Ga (Figure 5). Due to the flat shape of the crater floor, which could potentially have been the result of reworking processes long after the impact, a further degree of detail for this estimate was added by evaluating the age of the crater floor against that of the ejecta blanket, respectively, and obtaining a very close age for the two units. This therefore allows us to rule out the possibility of a substantial rejuvenation of the floor (on which the deposits examined here are superimposed) following an initial infill of material in the immediate post-impact phase (see Supporting Information S1).

This crater appears relevant for investigation due to the observation of many preserved water-related features contained within its rims. Specifically, we observed (a) fan-shaped depositional landforms on the crater floor, (b) short valleys carved on the crater walls, and (c) terraces.

The DEM shows, through planar view and cross sections, that the fan-shaped sedimentary bodies have flat tops that transition, at a consistent elevation of −4,050 m, into a steep frontal scarp. We interpreted deposits 1–3 (Figure 6b) as deltas, while we defined deposits 4–6 (Figures 6a and 6c) as putative deltas, as in the DEM they do not display such a clear slope break that marks the passage from the delta top to the frontal scarp and would indicate a delta front. We identified and mapped the feeding channels for each fan-shaped feature. The valley lengths are very short compared to global average valley lengths (Alemanno et al., 2018) and range from a minimum of 3 km to about 20 km. Other valleys missing a correlation with any deposits on the crater floor were also observed on the crater walls. All these valleys show steep walls, steep amphitheater-like headwalls, and the tendency to maintain a constant width or widen in the upstream direction. Most of these incised valleys also share common elevations of their head and tip locations. Valley heads are located around −2,900 m while their tips reach −3,750 m, and only a few isolated valleys show head or tip elevations falling within this specified range (Figure 6a). We did not observe an inlet valley, suggesting that a putative paleolake in this crater would have probably been fed by groundwater seepage, similar to lakes near Ares Vallis (Warner et al., 2010).

3.2. Water Volume

Valley tips and delta fronts are widely acknowledged as distinctive features that indicate the position of water levels at equilibrium in basin environments filled with water. In the studied crater, the elevation of the delta fronts (−4,050 m) does not coincide with the elevation of the transition point from feeder channel to depositional

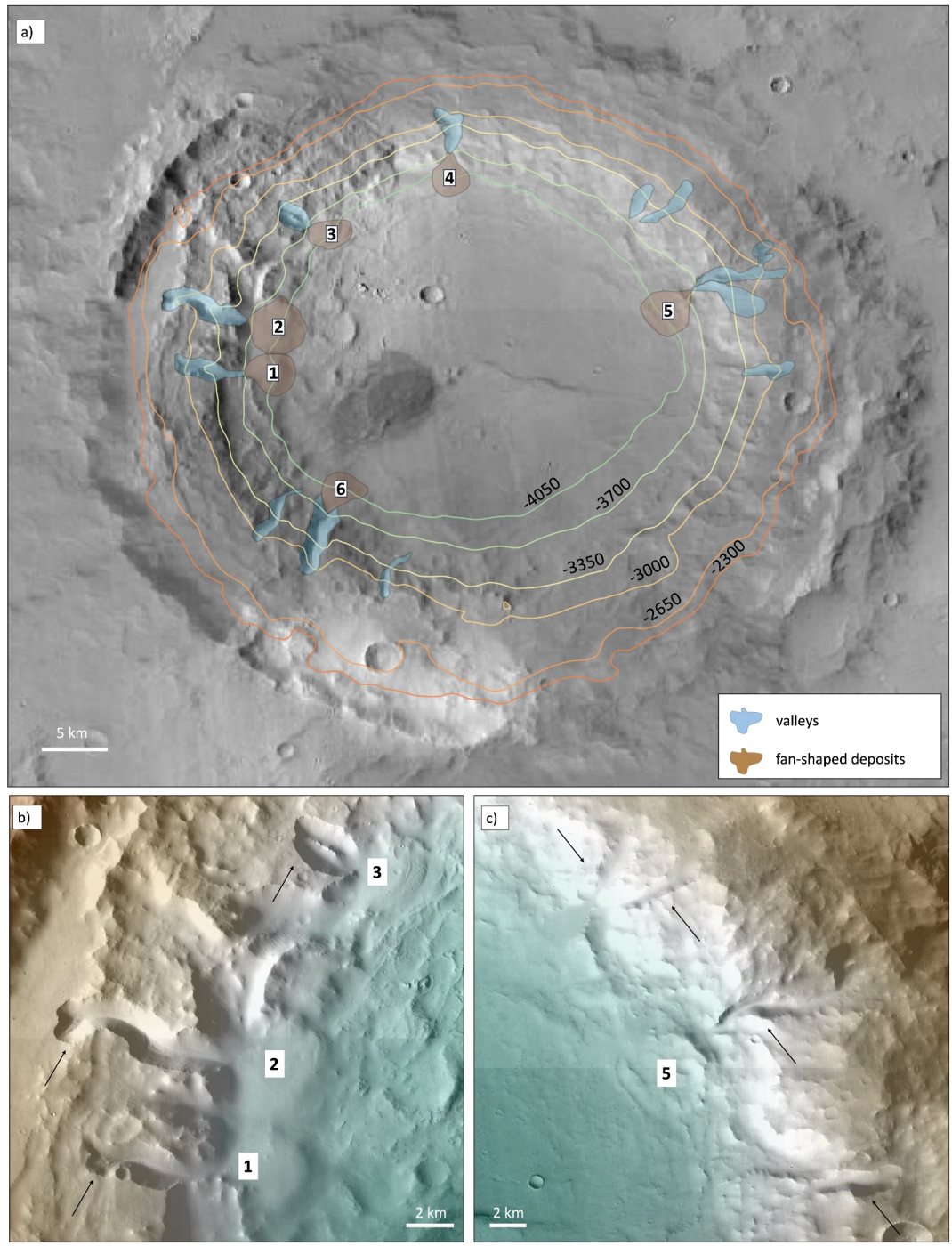

Figure 6. (a) CTX mosaic of the study area, with geomorphological features relevant to this study mapped in blue (valleys) and brown (fan-shaped deposits). Fan-shaped deposits are numbered for clear correspondence to the main text. (b) and (c) Close-up images (CTX) of valleys (indicated by black arrows) and fan-shaped deposits (identified by their progressive numbering) on both sides of the examined crater. Topography is represented with false colors, where blue areas indicate lower elevation and brown areas indicate higher elevation.

morphology (i.e., valley tip; −3,750 m). Therefore, it is likely that these two separate elevations represent the range within which the water level in the basin must have oscillated during the period of active water discharge through the channels. Accordingly, we calculated the volumes contained between the crater floor and these two boundary water levels that the basin experienced during its equilibrium phase before the cessation of water supply

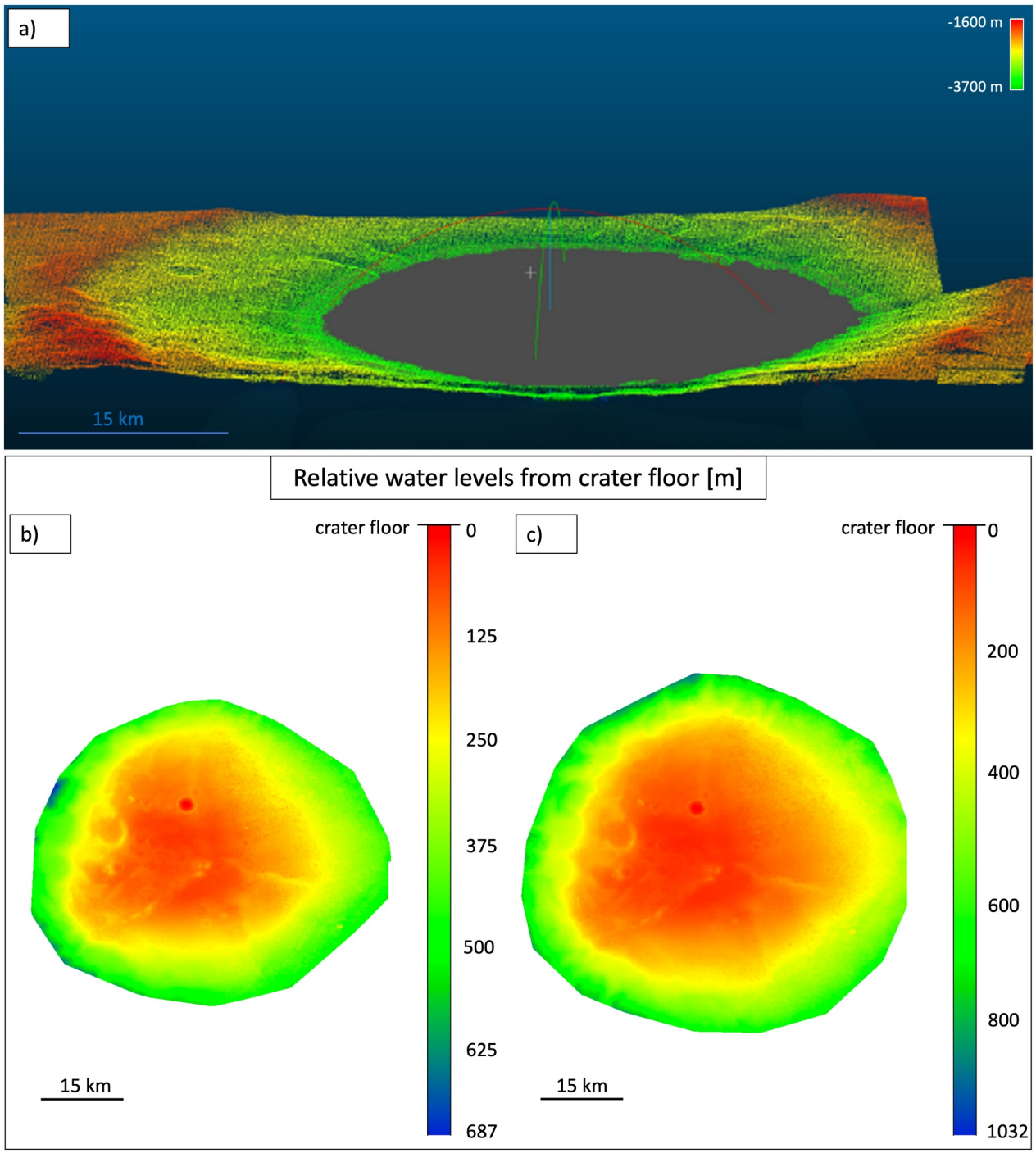

Figure 7. (a) Crater point cloud (CC false colors; corresponding absolute elevations are reported in the scale bar) intersects the gray plane crossing the valley tips providing a reconstruction of how the basin could have looked like when a stable body of water was present. Below, the two calculated boundary volumes are shown in planar view and the relative water level inside the crater is displayed through the color bars on the side. (b) Water volume underneath the delta front elevation is 280 km^3, corresponding to a water level estimated at around 690 m from the crater floor. (c) Water volume included below the valley tips elevation is 606 km^3, corresponding to a water level estimated at around 1,030 m from the crater floor.

(Figure 7). Specifically, the water volume present in the basin when the water level reached the delta fronts corresponds to c. 280 km^3 (Figure 7b), that is, 690 m from the crater floor, and c. 606 km^3, that is, 1,030 m from the crater floor, when the water level reached the valley tip (Figure 6c).

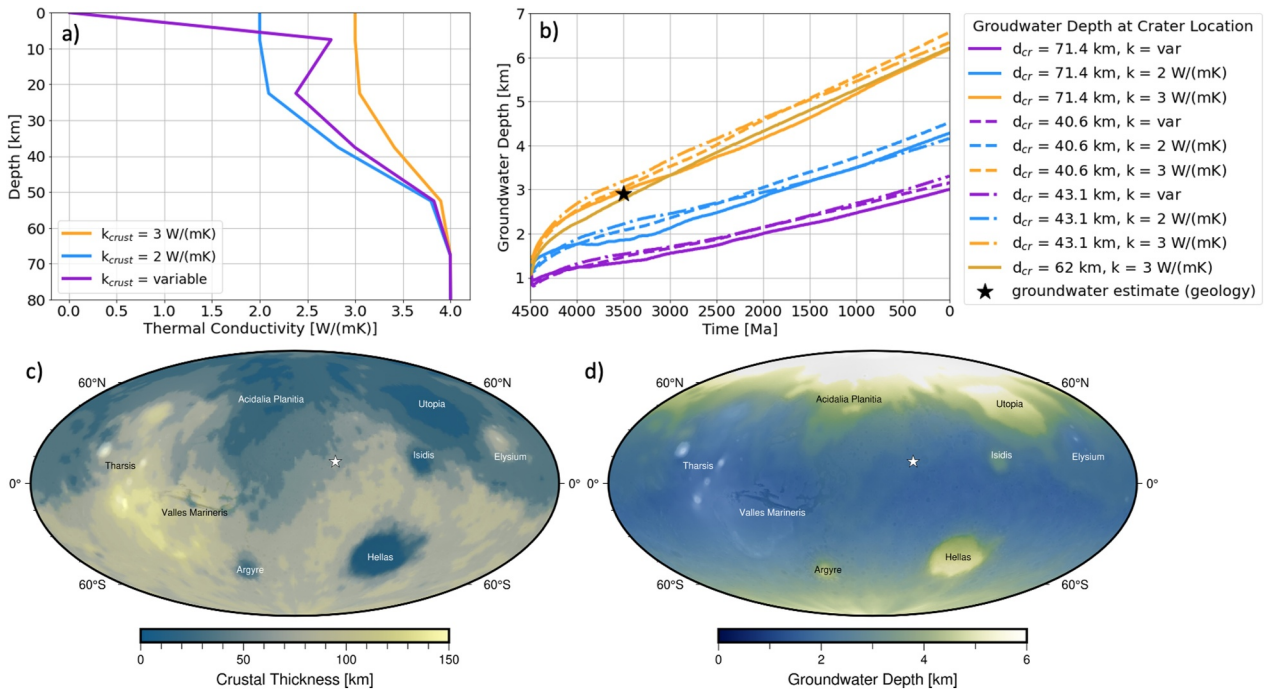

Figure 8. (a) Thermal conductivity profiles used in the geodynamical simulations. (b) Groundwater depth evolution through time based on results from models using various crustal thicknesses from Wieczorek et al. (2022) and crustal thermal conductivity values (see panel a). We note that the best-fit case using an average crustal thickness of 62 km coincides with one of the best-fit cases selected by Plesa et al. (2018), based on excellent agreement with constraints on the thermal state and interior structure of Mars. (c) Crustal thickness and (d) groundwater depth at 3.5 Ga obtained for the best-fit model in panel (b).

3.3. Thermal Modeling

We calculate the hypothetical groundwater depth at the time of crater formation by using our geodynamical models described in Section 2.3 and compare the temperature at each location across the planet with the melting temperature of water-ice. We compute the groundwater depth through time at the crater location and compare it with our groundwater depth estimates based on the elevation of the valley heads. We test different thermal conductivity values for the crust, and show the laterally averaged profiles that illustrate the average thermal conductivity values at each depth in Figure 8a. The thermal conductivity increases gradually from the crustal to the mantle values. This effect can be clearly seen for constant thermal conductivities in the crust and mantle, where a gradual transition between the values of the crust and those of the mantle can be observed (Figure 8a). A value between that of the crust and that of the mantle indicates the fact that the profile includes an average of both mantle and crustal material (blue and orange lines in Figure 8a). In the variable crustal conductivity case, the conductivity increases down to a depth of about 8 km due to a decrease in crustal porosity. Afterward, the effect of the temperature-dependence dominates, leading to a decrease in thermal conductivity. This is followed by an increase as the depth increases owing to the fact that more mantle material contributes to the average thermal conductivity until eventually the mantle value of 4 W/(mK) is reached. We find that models with a variable thermal conductivity of the crust predict the shallowest groundwater level, while models with a constant thermal conductivity of 3 W/(mK) show the deepest groundwater (Figure 8). This is explained by the fact that the lowest effective thermal conductivity and hence, the largest insulating effect is obtained by the models with a variable crustal thermal conductivity. In these models, the groundwater level at around 3.5 Ga is situated between 1.35 and 1.53 km depth at the crater location, whereas for models with a constant crustal thermal conductivity of 3 W/(mK) the groundwater level lies deeper than 2.79 km. The cases considering a crustal thermal conductivity of 2 W/(mK) show a groundwater depth of 1.85–2.22 km at the crater location, at 3.5 Ga, independent of the crustal thickness model used.

Figure 8c shows the crustal thickness and Figure 8d the corresponding depth of groundwater, from a model that matches remarkably well the groundwater depth based on the geological analyses. This model has an average crustal thickness of 62 km and a crustal thermal conductivity of 3 W/(mK) and is one of the best-fit models

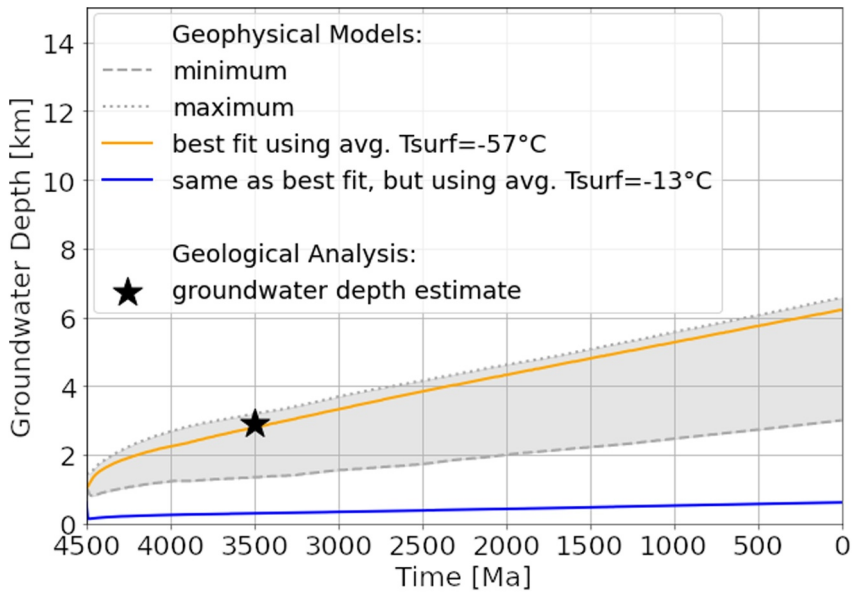

Figure 9. Groundwater depth with time summarized from the geodynamical models that use an average temperature of −57°C presented in Figure 7b, highlighting a best-fit model by an orange colored line. The blue line shows the groundwater depth from an additional model similar to the best-fit model but with an average surface temperature of −13°C.

selected by Plesa et al. (2018) based on constraints for the thermal state and interior structure of Mars from geophysical, geochemical, and geological data. The crater's location is indicated by a star symbol. The groundwater depth map shows a large degree of variability with 1 km or less in equatorial regions and more than 6 km at the north pole of Mars. The variations are controlled in part by the crustal thickness pattern (shallow groundwater depth in thick crustal regions beneath volcanic centers and deep groundwater level in regions covered by a thin crust, i.e., large impact basins) and in part by surface temperature variations (shallow groundwater table in warm equatorial regions and deeper groundwater depth in cold polar regions). The groundwater level in the Hack crater is close to the planetary average (difference of less than 1 km for all models tested here, see Supporting Information Data sets, https://doi.org/10.5281/zenodo.15267419), which makes this location an interesting location to understand the evolution of the global groundwater level on Mars.

4. Discussion

4.1. Geophysical Model Limitations and Future Steps

The surface temperature in our geodynamical models is on average −57°C and varies spatially with latitude, having warm temperatures at the equator and colder temperatures at the poles, but it does not vary through time. While the evolution of surface temperature will not affect the dynamics in the deep interior, it may affect the near-surface temperature gradient, leading to a shallower groundwater depth. Assuming a higher average surface temperature of −13°C at 3.5 Ga (Kite & Conway, 2024, their Figure 3) and shifting our surface temperature values, which include latitudinal variations, to match this higher average surface temperature, we rerun our best-case global 3D thermal evolution model (i.e., we rerun the best-fit model from Figure 8 with a higher surface temperature). The shift of the surface temperature to match a −13°C global average at 3.5 Ga results in a local value of −5°C at the crater location. For this scenario, the groundwater level shifts to a shallow depth of only −500 m at the crater location at 3.5 Ga (Figure 9). The groundwater depth obtained for a warmer surface temperature is much shallower compared to the heads of the valleys identified in our geological analyses, suggesting that either (a) the temperatures in the past were lower than those inferred from geological features caused by past warmer and wetter events, at least locally, or (b) shorter time-scale or spatial-scale fluctuations occurred (Kite & Conway, 2024), or (c) the groundwater was shallower but the valleys started at −2,900 m because there were no pathways for the water to flow and infill the crater. The latter scenario seems unlikely, because upon crater formation, fracturing is expected to occur and would have provided the necessary pathways for water flow.

A better definition of the surface temperature evolution, including local surface temperature variations, would require a coupling between geodynamical and atmospheric global circulation models, which is beyond the scope of this work but should be considered in future studies. We note that this coupling would introduce additional parameters with their own uncertainties that need to be carefully quantified.

Another source of uncertainty that exists for estimating the ground water depth from global geodynamical models is the presence of salts. In particular, perchlorates in eutectic concentrations dramatically reduce the melting temperature of water-ice and could shift the groundwater level closer to the surface (e.g., Clifford et al., 2010). Unfortunately, the presence and distribution of salts is difficult to constrain even on the Martian surface as orbital measurements are not sensitive enough to distinguish their signature (e.g., Carrier et al., 2020). However, a shallower groundwater level would have likely formed the valley heads at a shallower depth than that observed in this crater.

Groundwater flow, which was modeled in previous studies (Andrews-Hanna et al., 2010), could affect the distribution of groundwater depth on the planet. However, the permeability, which is a key parameter controlling the flow of groundwater, is poorly constrained and linked to the porosity and compressibility of the subsurface material (Andrews-Hanna et al., 2010). These properties of the subsurface could be strongly affected by the impact, and a better quantification of the impact related processes (formation of fractures, porosity build up or removal etc.) is necessary. Moreover, groundwater flow would require a careful coupling on different spatial and temporal scales between a water flow model with our thermal state estimates from the geodynamical thermal evolution models, which is beyond the scope of this study. Future modeling efforts will address this coupled scenario and assess the uncertainties introduced by additional parameters required by the water flow model.

4.2. Reconstruction of Water Availability

Hack crater displays numerous water-related features suggesting that during its evolution it must have experienced at least one period of intense water activity despite its formation postdates the Noachian period. Nevertheless, the crater is missing a connection with large-scale fluvial networks capable of surface runoff. Short valleys are instead found confined within the crater walls displaying: (a) semi-circular, theater-shaped heads that typically form when sufficient sediment is removed from the base of the headwall through water seepage and sediment discharge downstream to avoid clogging and blocking further channel retrograding erosion (Marra et al., 2015); and (b) widths that are mostly homogeneous along the valley or widening upstream, which also constitutes a morphological trait typical of sapping-dominated valleys (Kochel and Piper, 1986). These distinguishing morphologies, along with the presence of sediment accumulation at the tip of most valleys, suggest an interplay between groundwater seepage and mass-wasting processes during their formation. Groundwater seepage likely initiated the sapping processes by weakening the structural integrity of the headwall and mobilizing sediments, which were subsequently transported downstream. This seepage-induced instability triggered localized mass-wasting events, contributing to the ongoing valley evolution and the deposition of sediment in fan-shaped landforms at the valley tips.

When groundwater flow and seepage take place, outlet locations depend on the level of the groundwater table (Abrams et al., 2009). As the emergence of springs is connected to groundwater availability, it implies that the valley heads cannot grow above the groundwater level that generates them. Accordingly, the elevation of valley head locations in the studied crater can provide us with information about groundwater supply during the period of formation. Specifically, we observe that in 9 out of 12 mapped channels the valley head is located close to −2,900 m elevation, and the other 2 display heads at similar elevations or well below. Given this consistent behavior around the entire crater perimeter, it is possible to infer that the −2,900 m elevation level may represent the top of the groundwater table at the time when the respective landforms developed after the crater formation at around 3.5 Ga (Figure 5).

Further information on water availability within the crater can be drawn from the locations of valley tips and delta fronts, which are commonly accepted (e.g., Di Achille & Hynek, 2010) as marker morphologies representing the location of equipotential water levels in water-filled basins. Again, we observed an outstanding consistency across the whole study area where 10 out of 12 valleys terminate sharply at −3,750 m elevation, while the other two show tips at higher elevations. The complete absence of deeper channel excavation suggests that this location represents a transition zone, where erosional processes associated with subaerial conditions gave way to a subaqueous environment characterized by sediment deposition rather than further downcutting. Fan-shaped deposits

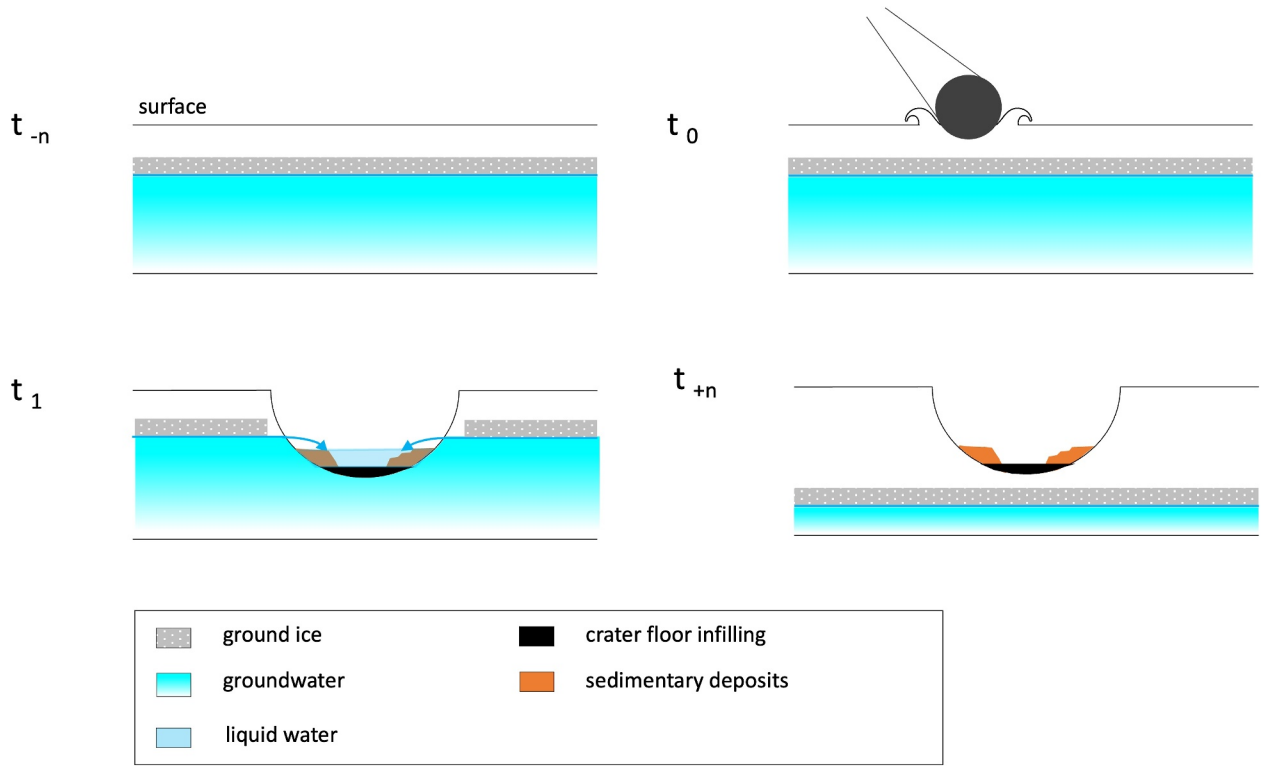

Figure 10. The main events spanning the aqueous history of the examined area, from crater formation to the present condition. t_{-n} = unperturbed pre-impact crust; t_0 = impact (3.5 Ga); t_1 = crater stabilizes and the floor is infilled immediately after, temperature is above the ground ice stability temperature, water sapping, valleys and fan-shaped deposits formation, the basin fills with water. t_{+n} = after t_1 the system cools down, the basin dries out, geomorphological features connected to water circulation are left in a subaerial environment and the ice and groundwater levels sink and adapt to the new local surficial roughness. At a later geologically relevant time in the climatic evolution of Mars, the planet cools and dries out leading to a regional drop in the water table.

located at the valley tips display various degrees of degradation, but well-preserved stepped deltas (De Toffoli et al., 2021) are visible inside the crater whose delta fronts (i.e., upper break in slope of the frontal scarp) are located at a consistent elevation of c. −4,050 m. This represents the lower point of transition from a subaerial to a subaqueous environment while water runoff from the water seepage was still active.

Features 1–3 (Figure 6a) have previously been interpreted as deltas (e.g., De Toffoli et al., 2021; Di Achille & Hynek, 2010; Salese et al., 2019), deposits 4–5 have been previously interpreted as deltas by Salese et al. (2019), and deposits 1–4 and 6 have been previously defined as "scarp-fronted deposits" (Irwin et al., 2005). Based on CTX and HiRISE imagery and local topography extracted from the DTM, we interpret deposits #1–3 and #6 as deltas, and deposit #4 (perhaps also #3) as a stepped delta. The origin of deposit #5 is less certain, and it is not clear whether it is a sedimentary body linked to an upstream valley. Stepped deltas were previously interpreted to form during rapid water level rise (De Villiers et al., 2013), which would seem consistent with the filling of a crater by drainage of an aquifer after an impact.

4.3. Timeline of Events Leading to Water Features Formation

Our investigations allow us to largely reconstruct a timeline of key events that shaped the examined area (Figure 10) starting from the formation of the studied crater at 3.5 Ga. One source of uncertainty for the relevance of data within a global evolutionary and climatic context remains the limited extent of the study area. However, it remains relevant to note what inferences can be drawn from the analysis of this crater with its unique characteristics and how they intertwine with the data already available to better understand the Martian groundwater evolution.

At that time, groundwater potentially existed in the subsurface at a depth of −2,900 m (elevation of the sapping valley heads extracted from the analysis of the DEM) or deeper. This is consistent with geodynamic models that

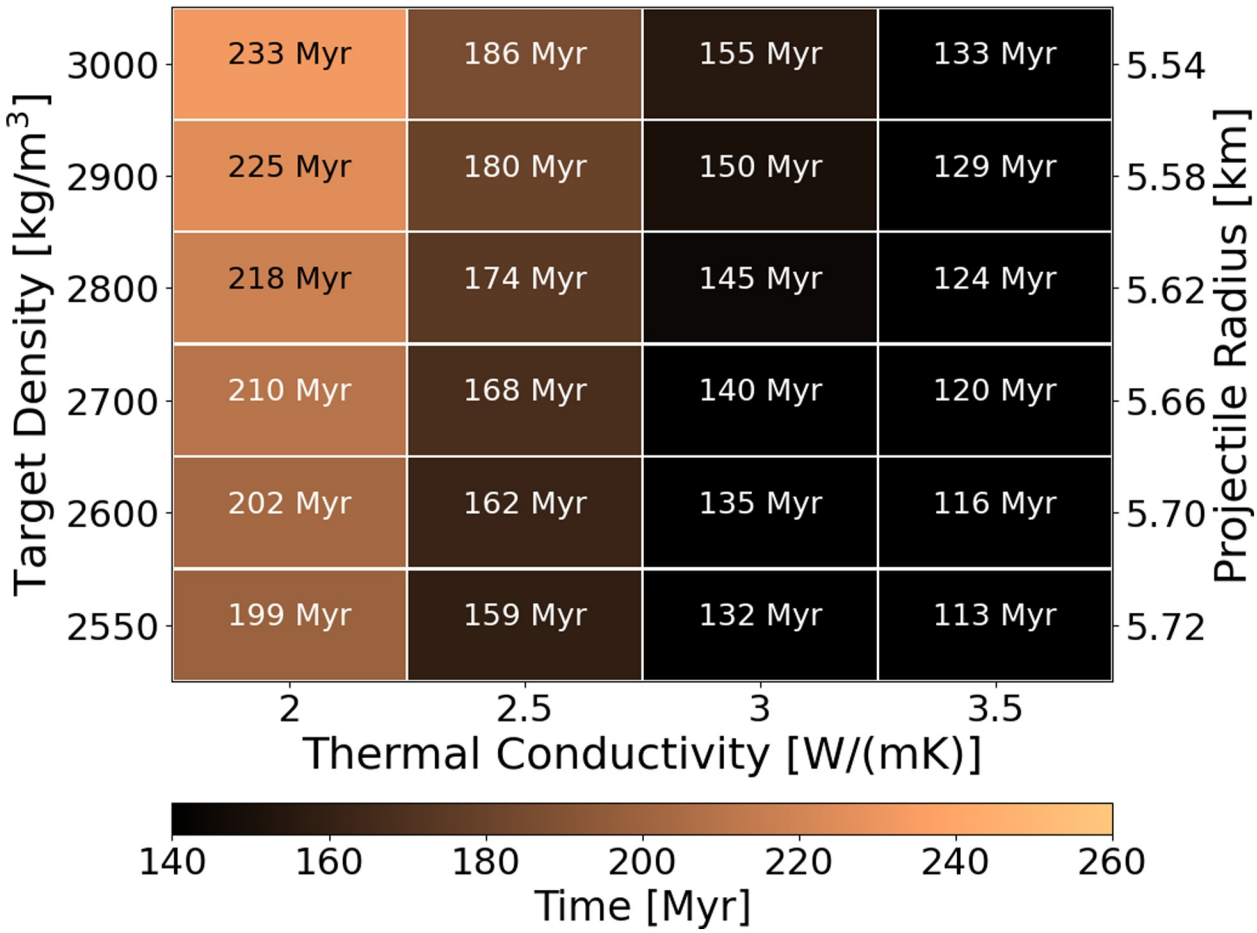

Figure 11. Time of conductive cooling of the heat anomaly introduced during the impact process. We use impact parameters relevant for Mars (impact velocity: 7 km/s, impact angle: 45°), and estimate the projectile diameter based on the basin size using the Pi-scaling (Impact Calculator. By H. Jay Melosh and Ross A. Beyer, https://pirlwww.lpl.arizona.edu/~rbeyer/crater_p.html). We tested a range of crustal densities (2,550–3,000 kg m^{-3}; Wieczorek et al., 2022) and crustal thermal conductivities (2.0–3.5 Wm^{-1}K^{-1}) to determine the time required to dissipate the heat introduced by the impact.

show favorable thermal conditions for liquid water to exist at that depth. We propose that the water table is shown to be flat on the sketch in Figure 10, t_{-n}. We propose that in the absence of crustal perturbations (i.e., large crustal thickness differences introduced by, e.g., impact basins) or local anomalies (heat anomalies due to crustal heat source anomalies, the local presence of salts etc.) it is reasonable to assume that the groundwater level in the area is roughly at the same depth. After the crater formation, fracturing of the crust created the necessary pathways which led to groundwater leakage into the crater. Assuming typical impact conditions for Mars (impact velocity of 7 km/s, impact angle of 45°) and a variety of thermophysical properties for the crust (crustal density between 2,550 kg m^{-3} and 3,000 kg m^{-3}, and thermal conductivity between 2 and 3.5 Wm^{-1}K^{-1}), the heat anomaly introduced by the impact lasts for a couple of hundreds of Myrs (Figure 11) preventing an immediate freezing or sublimation and allowing for hydrothermal activity (Abramov & Kring, 2005). Furthermore, the exceptionally good match between geomorphological observations and the expected groundwater depth obtained through modeling suggests that the crater infill likely took place shortly after the impact when the thermal state of the subsurface allowed for shallow groundwater levels compared to present day conditions. In this scenario, groundwater flowed from the subsurface toward the basin, triggering water sapping and sediment mobilization. After this stage, (a) the water input stopped due to exhaustion of the groundwater reservoir (assuming no globally interconnected aquifer, Harrison & Grimm, 2009) or because groundwater conduits into the crater become blocked by top-down freezing; (b) the water already present in the basin got lost to the ground and atmosphere; (c) the groundwater table reached a deeper level due to the lesser insulation because of the thinner crust caused by the presence of the crater (Figure 10: t_{+n}), eventually arriving at a scenario comparable to that currently observed. In

this context, combining this reconstruction with the calculations of water volume in the lake can provide a useful basis for future investigations into currently unknown or poorly constrained parameters crucial for elucidating the specific formation processes and ground conditions that sustained the lake formation and existence. We cannot rule out a possible contribution to the lake formation system by melting putative ground ice. Despite the age and the depth of the crater being in favor of a scenario mainly fed by groundwater seepage, an unknown portion of the water leaked into the basin might have come from ground ice melting as a consequence of the impact, as suggested elsewhere to explain the existence of Martian lakes in the late Hesperian and even the Amazonian (Hauber et al., 2013). To the same extent, as temperatures dropped in later stages of evolution, it is possible that the freezing of the groundwater, and thus the formation of new ground ice, may have then obstructed groundwater flow even before the water table retreated to greater depths. However, this specific scenario needs to be investigated in future studies.

Although the data collected in the study area are local and spatially limited, it can be inferred—with all due caution—that the climate at 3.5 Ga was not characterized by widespread liquid surface water, as we do not see any valleys that would have been fed by precipitation and surface runoff in the crater and its surrounding. On the other hand, the existence of sapping valleys and associated deltaic deposits point to the existence of an aquifer in the uppermost few kilometers of the martian crust, which leaked into the newly created depression after the impact at ∼3.5 Ga. Although surface conditions were not as wet as in the Noachian anymore, the planet was still in a thermal state that allowed liquid groundwater at relatively shallow levels. A scenario like this would be consistent with an atmosphere that was already thinner than that in the Nochian-Early Hesperian, although we cannot quantitatively constrain it. A relatively low paleo-pressure in the Hesperian at ∼3.5 Ga was also postulated by Kite et al. (2014) on the basis of impact crater diameters as proxies for atmospheric density, and by Bristow et al. (2017) on the basis of mineralogical observations in Gale crater.

5. Conclusions

The results of our study allow us to reconstruct the evolution, from formation to desiccation, of a Martian closed lake filled by groundwater seepage instead of surface runoff. After the impact crater formation ∼3.5 Ga, the newly formed basin filled with groundwater via seepage, and subsequent aqueous activity led to the incision of valleys by sapping processes and deposition of fan-shaped deposits. Because groundwater seepage was most likely the main water input in the basin, we constrained the maximum groundwater table elevation to approximately −2,900 m by measuring the elevation of the valley heads along the crater perimeter. Upon cessation of water inputs, the basin dried out, and the water-related morphologies were exposed to the erosion in a subaerial environment.

The assessment of the wider implications of such reconstruction needs to consider the regional context, as our observations apply only to the study area. The abundance and types of water-related features observed at this site are not found in other nearby craters, indicating that this specific location may uniquely preserve these features. Several authors have proposed the existence of a planet-wide groundwater system on Mars (e.g., Andrews-Hanna et al., 2010; Clifford, 1993; Salese et al., 2019; Treiman, 2008) and the water level inferred in the examined crater is compatible with the Deuteronilus shoreline level (Citron et al., 2018; Clifford & Parker, 2001; Ivanov et al., 2017; Perron et al., 2007; Sholes et al., 2021). However, it is important to note that the evidence collected from this single location is not sufficient to definitively constrain groundwater behavior on a regional or global scale (cf., Hauber et al., 2013). Nevertheless, the lack of evidence of post-impact surface runoff in combination with groundwater seepage point to a climate which did not sustain large amounts of liquid surface water on a global scale, but still allowed for liquid groundwater less than 3 km deep in the crust. This would be consistent with the notion that the impact that caused the crater at 3.5 Ga occurred in a critical transition time in Mars' history, between the earlier wetter periods which enabled the formation of dendritic valley networks indicative of sustained surface runoff, and the cold and arid climate prevailing through the Amazonian.

Data Availability Statement

The CTX DEMs used in this work are available from the PDS Geosciences Node (http://ode.rsl.wustl.edu/). The HiRISE images used in this work for qualitative analyses (ESP_016696_2085 and ESP_016485_2085) can be downloaded in the JP2 format from https://hirise.lpl.arizona.edu/. The THEMIS nighttime infrared mosaic was

added as a WMS layer on QGIS (see https://stac.astrogeology.usgs.gov/docs/tutorials/qgis_add_wms/). For mapping and measurements, the QGIS software was used, which is a free and open source Geographic Information System (https://www.qgis.org/en/site/index.html). For the water volume estimates, we used the open source CloudCompare software (https://www.danielgm.net/cc/). Groundwater depths computed here and presented in Figure 8 are available as tabulated data in the supplementary online material. The data produced in this paper are provided as supplementary information in De Toffoli et al. (2025).

Acknowledgments
B.D.T. is supported by the European Union —NextGenerationEU and by the 2023 STARS Grants@Unipd programme HECATE. We thank two anonymous reviewers for their insightful comments that helped improve an earlier version of this manuscript. We also thank the editor Deanne Rogers for handling our paper. Open Access funding enabled and organized by Projekt DEAL.

References

Abramov, O., & Kring, D. A. (2005). Impact-induced hydrothermal activity on early Mars. *Journal of Geophysical Research*, *110*(E12), E12S09. https://doi.org/10.1029/2005JE002453

Abrams, D. M., Lobkovsky, A. E., Petroff, A. P., Straub, K. M., McElroy, B., Mohrig, D. C., et al. (2009). Growth laws for channel networks incised by groundwater flow. *Nature Geoscience*, *2*(3), 193–196. https://doi.org/10.1038/ngeo432

Alemanno, G., Orofino, V., & Mancarella, F. (2018). Global map of Martian fluvial systems: Age and total eroded volume estimations. *Earth and Space Science*, *5*, 560–577. https://doi.org/10.1029/2018EA00036

Andrews-Hanna, J. C., Zuber, M. T., Arvidson, R. E., & Wiseman, S. M. (2010). Early Mars hydrology: Meridiani playa deposits and the sedimentary record of Arabia Terra. *Journal of Geophysical Research*, *115*(E6), E06002. https://doi.org/10.1029/2009je003485

Becker, K. J., Anderson, J. A., Sides, S. C., Miller, E. A., Eliason, E. M., & Keszthelyi, L. P. (2007). Processing HiRISE images using ISIS3. In *38th Annual Lunar and Planetary Science Conference* (Vol. 1338, p. 1779).

Beyer, R. A., Alexandrov, O., & McMichael, S. (2018). The Ames Stereo Pipeline: NASA's open source software for deriving and processing terrain data. *Earth and Space Science*, *5*(9), 537–548. https://doi.org/10.1029/2018ea000409

Bramson, A. M., Byrne, S., Putzig, N. E., Sutton, S., Plaut, J. J., Brothers, T. C., & Holt, J. W. (2015). Widespread excess ice in Arcadia Planitia, Mars. *Geophysical Research Letters*, *42*(16), 6566–6574. https://doi.org/10.1002/2015GL064844

Bristow, T. F., Haberle, R. M., Blake, D. F., Des Marais, D. J., Eigenbrode, J. L., Fairén, A. G., et al. (2017). Low Hesperian P_{CO2} constrained from in situ mineralogical analysis at Gale Crater, Mars. *Proceedings of the National Academy of Sciences*, *114*(9), 2166–2170. https://doi.org/10.1073/pnas.1616649114

Cabrol, N. A., & Grin, E. A. (2001). The evolution of lacustrine environments on Mars: Is Mars only hydrologically dormant? *Icarus*, *149*(2), 291–328. https://doi.org/10.1006/icar.2000.6530

Carrier, B. L., Beaty, D. W., Meyer, M. A., Blank, J., Chou, L., DasSarma, S., et al. (2020). Mars extant life: What's next? Conference report. *Astrobiology*, *20*(6), 785–814. https://doi.org/10.1089/ast.2020.2237

Christensen, P. R., Jakosky, B. M., Kieffer, H. H., Malin, M. C., McSween, H. Y., Nealson, K., et al. (2004). The thermal emission imaging system (THEMIS) for the Mars 2001 Odyssey Mission. *Space Science Reviews*, *110*(1/2), 85–130. https://doi.org/10.1023/b:spac.0000021008.16305.94

Citron, R. I., Manga, M., & Hemingway, D. J. (2018). Timing of oceans on Mars from shoreline deformation. *Nature*, *555*(7698), 643–646. https://doi.org/10.1038/nature26144

Clauser, C., & Huenges, E. (1995). Thermal conductivity of rocks and minerals. In A. Brandt & H. Fernando (Eds.), *Rock Physics and Phase Relations: A Handbook of Physical Constants* (Vol. 3, pp. 105–126). AGU Ref. Shelf. https://doi.org/10.1029/rf003p0105

Clifford, S. M. (1993). A model for the hydrologic and climate behavior of water on Mars. *Journal of Geophysical Research*, *98*(E6), 10973–11016. https://doi.org/10.1029/93je00225

Clifford, S. M., Lasue, J., Heggy, E., Boisson, J., McGovern, P., & Max, M. D. (2010). Depth of the Martian cryosphere: Revised estimates and implications for the existence and detection of subpermafrost groundwater. *Journal of Geophysical Research*, *115*(E7), E07001. https://doi.org/10.1029/2009JE003462

Clifford, S. M., & Parker, T. J. (2001). The evolution of the Martian hydrosphere: Implications for the fate of a primordial ocean and the current state of the Northern Plains. *Icarus*, *154*(1), 40–79. https://doi.org/10.1006/icar.2001.6671

Craddock, R. A., & Howard, A. D. (2002). The case for rainfall on a warm, wet early Mars. *Journal of Geophysical Research*, *107*(E11), 21-1–21-36. https://doi.org/10.1029/2001je001505

Davis, J. M., Balme, M., Grindrod, P. M., Williams, R. M. E., & Gupta, S. (2016). Extensive Noachian fluvial systems in Arabia Terra: Implications for early Martian climate. *Geology*, *44*(10), 847–850. https://doi.org/10.1130/g38247.1

De Toffoli, B., Plesa, A., Hauber, E., & Breuer, D. (2021). Delta deposits on Mars: A global perspective. *Geophysical Research Letters*, *48*(17), 1–10. https://doi.org/10.1029/2021gl094271

De Toffoli, B., Plesa, A.-C., Luzzi, E., & Hauber, E. (2025). Groundwater sapping in a Martian crater: Geologic evidence and geophysical modeling of groundwater stability [Dataset]. *Zenodo*. https://doi.org/10.5281/zenodo.15267419

De Villiers, G., Kleinhans, M. G., & Postma, G. (2013). Experimental delta formation in crater lakes and implications for interpretation of Martian deltas. *Journal of Geophysical Research: Planets*, *118*(4), 651–670. https://doi.org/10.1002/jgre.20069

De Villiers, G., Kleinhans, M. G., Postma, G., Hauber, E., de Jong, S., & de Boer, P. L. (2009). Types of Martian fan-shaped sedimentary deposits. In *Lunar and Planetary Science Conference* (Vol. 40). abstract #1901.

Di Achille, G., & Hynek, B. M. (2010). Ancient Ocean on Mars supported by global distribution of deltas and valleys. *Nature Geoscience*, *3*(7), 459–463. https://doi.org/10.1038/ngeo891

Dickeson, Z. I., Grindrod, P. M., Davis, J. M., Crawford, I., & Balme, M. (2022). Hydrological history of a palaeolake and valley system on the planetary dichotomy in Arabia Terra, Mars. *Journal of Geophysical Research: Planets*, *127*(12), e2021JE007152. https://doi.org/10.1029/2021je007152

Dickson, J. L., Ehlmann, B. L., Kerber, L. H., & Fassett, C. I. (2023). Release of the global CTX mosaic of Mars: An experiment in information preserving image data processing. In *54th Lunar and Planetary Science Conference*. Retrieved from https://www.hou.usra.edu/meetings/lpsc2023/pdf/2353.pdf

Dickson, J. L., Kerber, L., Fassett, C. I., & Ehlmann, B. L. (2018). A global, blended CTX mosaic of Mars with vectorized seam mapping: A new mosaicking pipeline using principles of non-destructive image editing. In *Lunar and Planetary Science Conference*.

Di Pietro, I., Schmidt, G., Tangari, A. C., Salese, F., Silvestro, S., Fairén, A. G., et al. (2023). Groundwater-controlled deposition of equatorial layered deposits in central Arabia Terra, Mars. *Journal of Geophysical Research: Planets*, *128*(3), e2022JE007504. https://doi.org/10.1029/2022JE007504

Dohm, J. M., Barlow, N. G., Anderson, R. C., Williams, J. P., Miyamoto, H., Ferris, J. C., et al. (2007). Possible ancient giant basin and related water enrichment in the Arabia Terra province, Mars. *Icarus*, *190*(1), 74–92. https://doi.org/10.1016/j.icarus.2007.03.006

Federal Geographic Data Committee [prepared for the Federal Geographic Data Committee by the U.S. Geological Survey]. (2006). FGDC Digital Cartographic Standard for Geologic Map Symbolization. Federal Geographic Data Committee Document Number FGDC-STD-013-2006 (p. 290). 2 plates.

Fergason, R. L., Hare, T. M., & Laura, J. (2018). *HRSC and MOLA Blended Digital Elevation Model at 200m v2*, *Astrogeology PDS Annex*. U.S. Geological Survey. Retrieved from https://astrogeology.usgs.gov/search/map/mars_mgs_mola_mex_hrsc_blended_dem_global_200m

Gilbert, G. K. (1885). The topographic features of lake shores. *United States Geological Survey Annual Report*, *5*, 75–123.

Goudge, T. A., Aureli, K. L., Head, J. W., Fassett, C. I., & Mustard, J. F. (2015). Classification and analysis of candidate impact crater-hosted closed-basin lakes on Mars. *Icarus*, *260*, 245–367. https://doi.org/10.1016/j.icarus.2015.07.026

Harrison, K. P., & Grimm, R. E. (2009). Regionally compartmented groundwater flow on Mars. *Journal of Geophysical Research*, *114*(E4), E04004. https://doi.org/10.1029/2008JE003300

Hartmann, W. K., & Neukum, G. (2001). Cratering chronology and the evolution of Mars. *Space Science Reviews*, *96*, 165–194. https://doi.org/10.1007/978-94-017-1035-0_6

Hauber, E., Gwinner, K., Kleinhans, M., Reiss, D., Di Achille, G., Ori, G.-G., et al. (2009). Sedimentary deposits in Xanthe Terra: Implications for the ancient climate on Mars. *Planetary and Space Science*, *57*(8–9), 944–957. https://doi.org/10.1016/j.pss.2008.06.009

Hauber, E., Platz, T., Reiss, D., Le Deit, L., Kleinhans, M. G., Marra, W. A., et al. (2013). Asynchronous formation of Hesperian and Amazonian-aged deltas on Mars and implications for climate. *Journal of Geophysical Research: Planets*, *118*(7), 1529–1544. https://doi.org/10.1002/jgre.20107

Irwin, R. P., Howard, A. D., Craddock, R. A., & Moore, J. M. (2005). An intense terminal epoch of widespread fluvial activity on early Mars. 2. Increased runoff and paleolake development. *Journal of Geophysical Research*, *110*(E12), E12S15. https://doi.org/10.1029/2005JE002460

Ivanov, B., Neukum, G., & Wagner, R. (2001). Size-frequency distributions of planetary impact craters and asteroids. In *Collisional processes in the solar system* (pp. 1–34). Springer. https://doi.org/10.1007/978-94-010-0712-2_1

Ivanov, M. A., Erkeling, G., Hiesinger, H., Bernhardt, H., & Reiss, D. (2017). Topography of the Deuteronilus contact on Mars: Evidence for an ancient water/mud ocean and long-wavelength topographic readjustments. *Planetary and Space Science*, *144*, 49–70. https://doi.org/10.1016/j.pss.2017.05.012

Kieffer, H. H. (2013). Thermal model for analysis of Mars infrared mapping. *Journal of Geophysical Research: Planets*, *118*(3), 451–470. https://doi.org/10.1029/2012JE004164

Kite, E., Williams, J.-P., Lucas, A., & Aharonson, O. (2014). Low palaeopressure of the martian atmosphere estimated from the size distribution of ancient craters. *Nature Geoscience*, *7*(5), 335–339. https://doi.org/10.1038/ngeo2137

Kite, E. S., & Conway, S. (2024). Geological evidence for multiple climate changes on Early Mars. *Nature Geoscience*, *17*(1), 10–19. https://doi.org/10.1038/s41561-023-01349-2

Knapmeyer-Endrun, B., Panning, M. P., Bissig, F., Joshi, R., Khan, A., Kim, D., et al. (2021). Thickness and structure of the martian crust from InSight seismic data. *Science*, *373*(6553), 438–443. https://doi.org/10.1126/science.abf8966

Kochel, R. C., & Piper, J. F. (1986). Morphology of large valleys on Hawaii: Evidence for groundwater sapping and comparisons with Martian valleys. *Journal of Geophysical Research*, *91*(B13), E175. https://doi.org/10.1029/jb091ib13p0e175

Malin, M. C., Bell, J. F., Cantor, B. A., Caplinger, M. A., Calvin, W. M., Clancy, R. T., et al. (2007). Context camera investigation on board the Mars Reconnaissance Orbiter. *Journal of Geophysical Research*, *112*(E5), E05S04. https://doi.org/10.1029/2006JE002808

Mangold, N., Quantin, C., Ansan, V., Delacourt, C., & Allemand, P. (2004). Evidence for precipitation on Mars from dendritic valleys in the Valles Marineris area. *Science*, *305*(5680), 78–81. https://doi.org/10.1126/science.1097549

Marra, W. A., McLelland, S. J., Parsons, D. R., Murphy, B. J., Hauber, E., & Kleinhans, M. G. (2015). Groundwater seepage landscapes from distant and local sources in experiments and on Mars. *Earth Surface Dynamics*, *3*(3), 389–408. https://doi.org/10.5194/esurf-3-389-2015

McEwen, A. S., Eliason, E. M., Bergstrom, J. W., Bridges, N. T., Hansen, C. J., Delamere, W. A., et al. (2007). Mars reconnaissance orbiter's high resolution imaging science experiment (HiRISE). *Journal of Geophysical Research*, *112*(E5), E05S02. https://doi.org/10.1029/2005je002605

Mège, D., Gurgurewicz, J., Massironi, M., Pozzobon, R., Tognon, G., Pajola, M., et al. (2023). Hydrothermal alteration of ultramafic rocks in Ladon basin, Mars—Insights from CaSSIS, HiRISE, CRISM, and CTX. *Journal of Geophysical Research: Planets*, *128*(1), e2022JE007223. https://doi.org/10.1029/2022JE007223

Michael, G. G. (2013). Planetary surface dating from crater size–frequency distribution measurements: Multiple resurfacing episodes and differential isochron fitting. *Icarus*, *226*(1), 885–890. https://doi.org/10.1016/j.icarus.2013.07.004

Milliken, R. E., Mustard, J. F., Poulet, F., Bibring, J., & Langevin, Y. (2005). Estimating the absolute water content of Arabia Terra using Mars Express OMEGA data. In *AGU Fall Meeting Abstracts* (Vol. 2005, p. P14A-02).

Mirino, M. (2022). *Ancient River Channels in Arabia Terra, Mars* (PhD thesis). The Open University. https://doi.org/10.21954/ou.ro.000148c5

Moore, J. M., & Howard, A. D. (2005). Large alluvial fans on Mars. *Journal of Geophysical Research*, *110*(E4), E04005. https://doi.org/10.1029/2004JE002352

Morgan, A. M., Howard, A. D., Hobley, D. E., Moore, J. M., Dietrich, W. E., Williams, R. M. E., et al. (2014). Sedimentology and climatic environment of alluvial fans in the Martian Saheki crater and a comparison with terrestrial fans in the Atacama Desert. *Icarus*, *229*, 131–156. https://doi.org/10.1016/j.icarus.2013.11.007

Morgan, A. M., Wilson, S. A., & Howard, A. D. (2022). The global distribution and morphologic characteristics of fan-shaped sedimentary landforms on Mars. *Icarus*, *385*, 115137. https://doi.org/10.1016/j.icarus.2022.115137

Ohring, G., & Mariano, J. (1968). Seasonal and latitudinal variations of the average surface temperature and vertical temperature profile on Mars. *Journal of the Atmospheric Sciences*, *25*(5), 673–681. https://doi.org/10.1175/1520-0469(1968)025<0673:salvot>2.0.co;2

Ori, G. G., Marinangeli, L., & Baliva, A. (2000). Terraces and Gilbert-type deltas in crater lakes in Ismenius Lacus and Memnonia (Mars). *Journal of Geophysical Research*, *105*(E7), 17629–17641. https://doi.org/10.1029/1999JE001219

Ori, G. G., Marinangeli, L., & Komatsu, G. (2000). Martian paleolacustrine environments and their geological constrains on drilling operations for exobiological research. *Planetary and Space Science*, *48*(11), 1027–1034. https://doi.org/10.1016/s0032-0633(00)00076-3

Palucis, M. C., Dietrich, W. E., Williams, R. M., Hayes, A. G., Parker, T., Sumner, D. Y., et al. (2016). Sequence and relative timing of large lakes in Gale crater (Mars) after the formation of Mount Sharp. *Journal of Geophysical Research: Planets*, *121*(3), 472–496. https://doi.org/10.1002/2015je004905

Penasa, L., Massironi, M., Simioni, E., Franceschi, M., Naletto, G., Ferrari, S., et al. (2021). Application of implicit 3D modeling to reconstruct the layered structure of the comet 67P. In *3D Digital Geological Models: From Terrestrial Outcrops to Planetary Surfaces*. Wiley. https://doi.org/10.1002/9781119313922.ch1

Perron, J. T., Mitrovica, J. X., Manga, M., Matsuyama, I., & Richards, M. A. (2007). Evidence for an ancient Martian ocean in the topography of deformed shorelines. *Nature*, *447*(7146), 840–843. https://doi.org/10.1038/nature05873

Plesa, A.-C., Grott, M., Tosi, N., Breuer, D., Spohn, T., & Wieczorek, M. A. (2016). How large are present-day heat flux variations across the surface of Mars? *Journal of Geophysical Research: Planets*, *121*(12), 2386–2403. https://doi.org/10.1002/2016JE005126

Plesa, A.-C., Padovan, S., Tosi, N., Breuer, D., Grott, M., Wieczorek, M. A., et al. (2018). The thermal state and interior structure of Mars. *Geophysical Research Letters*, *45*(22), 12198–12209. https://doi.org/10.1029/2018GL080728

Plesa, A. C., Wieczorek, M., Knapmeyer, M., Rivoldini, A., Walterova, M., & Breuer, D. (2022). Interior dynamics and thermal evolution of Mars–a geodynamic perspective. *Geophysical Exploration of the Solar System*, *63*, 179–230. https://doi.org/10.1016/bs.agph.2022.07.005

Pondrelli, M., Rossi, A. P., Le Deit, L., Fueten, F., van Gasselt, S., Glamoclija, M., et al. (2015). Equatorial layered deposits in Arabia Terra, Mars: Facies and process variability. *Bulletin*, *127*(7–8), 1064–1089.

Pondrelli, M., Rossi, A. P., Le Deit, L., Schmidt, G., Pozzobon, R., Hauber, E., & Salese, F. (2019). Groundwater control and process variability on the equatorial layered deposits of Kotido Crater, Mars. *Journal of Geophysical Research: Planets*, *124*(3), 779–800. https://doi.org/10.1029/2018je005656

Poulet, F., Bibring, J. P., Mustard, J. F., Gendrin, A., Mangold, N., Langevin, Y., et al. (2005). Phyllosilicates on Mars and implications for early Martian climate. *Nature*, *438*(7068), 623–627. https://doi.org/10.1038/nature04274

Salese, F., McMahon, W. J., Balme, M. R., Ansan, V., Davis, J. M., & Kleinhans, M. G. (2020). Sustained fluvial deposition recorded in Mars' Noachian stratigraphic record. *Nature Communications*, *11*(1), 2067. https://doi.org/10.1038/s41467-020-15622-0

Salese, F., Pondrelli, M., Neeseman, A., Schmidt, G., & Ori, G. G. (2019). Geological evidence of planet-wide groundwater system on Mars. *Journal of Geophysical Research: Planets*, *124*(2), 374–395. https://doi.org/10.1029/2018JE005802

Schmidt, G., Luzzi, E., Franchi, F., Selepeng, A. T., Hlabano, K., & Salvini, F. (2023). Structural influences on groundwater circulation in the Makgadikgadi salt pans of Botswana? Implications for martian playa environments. *Frontiers in Astronomy and Space Sciences*, *10*, 1108386. https://doi.org/10.3389/fspas.2023.1108386

Schmidt, G., Luzzi, E., Rossi, A. P., Pondrelli, M., Apuzzo, A., & Salvini, F. (2022). Protracted hydrogeological activity in Arabia Terra, Mars: Evidence from the structure and mineralogy of the layered deposits of Becquerel crater. *Journal of Geophysical Research: Planets*, *127*(9), e2022JE007320. https://doi.org/10.1029/2022je007320

Seipold, U. (1998). Temperature dependence of thermal transport properties of crystalline rocks: A general law. *Tectonophysics*, *291*(1–4), 161–171. https://doi.org/10.1016/S0040-1951(98)00037-7

Sholes, S., Dickeson, Z., Montgomery, D., & Catling, D. (2021). Data For: Where are Mars' hypothesized ocean shorelines? Large lateral and topographic offsets between different versions of Paleoshoreline maps. *Journal of Geophysical Research: Planets*, *126*(5), e2020JE006486. https://doi.org/10.1029/2020JE006486

Smith, D. E., Zuber, M. T., Frey, H. V., Garvin, J. B., Head, J. W., Muhleman, D. O., et al. (2001). Mars orbiter laser altimeter: Experiment summary after the first year of global mapping of Mars. *Journal of Geophysical Research*, *106*(E10), 23689–23722. https://doi.org/10.1029/2000je001364

Stähler, S. C., Khan, A., Banerdt, W. B., Lognonné, P., Giardini, D., Ceylan, S., et al. (2021). Seismic detection of the martian core. *Science*, *373*(6553), 443–448. https://doi.org/10.1126/science.abi7730

Tanaka, K. L., Robbins, S. J., Fortezzo, C. M., Skinner, J. A., & Hare, T. M. (2014). The digital global geologic map of Mars: Chronostratigraphic ages, topographic and crater morphologic characteristics, and updated resurfacing history. *Planetary and Space Science*, *95*, 11–24. https://doi.org/10.1016/j.pss.2013.03.006

Treiman, A. H. (2008). Ancient groundwater flow in the Valles Marineris on Mars inferred from fault trace ridges. *Nature Geoscience*, *1*(3), 181–183. https://doi.org/10.1038/ngeo131

Warner, N., Gupta, S., Lin, S.-Y., Kim, J.-R., Muller, J.-P., & Morley, J. (2010). Late Noachian to Hesperian climate change on Mars: Evidence of episodic warming from transient crater lakes near Ares Vallis. *Journal of Geophysical Research*, *115*(E6), E06013. https://doi.org/10.1029/2009JE003522

Wieczorek, M. A., Broquet, A., McLennan, S. M., Rivoldini, A., Golombek, M., Antonangeli, D., et al. (2022). InSight constraints on the global character of the Martian crust. *Journal of Geophysical Research: Planets*, *127*(5), e2022JE007298. https://doi.org/10.1029/2022JE007298

Wordsworth, R., Forget, F., Millour, E., Head, J. W., Madeleine, J. B., & Charnay, B. (2013). Global modelling of the early martian climate under a denser CO_2 atmosphere: Water cycle and ice evolution. *Icarus*, *222*(1), 1–19. https://doi.org/10.1016/j.icarus.2012.09.036

Zabrusky, K., Andrews-Hanna, J. C., & Wiseman, S. M. (2012). Reconstructing the distribution and depositional history of the sedimentary deposits of Arabia Terra, Mars. *Icarus*, *220*(2), 311–330. https://doi.org/10.1016/j.icarus.2012.05.007

Zaki, A. S., Pain, C. F., Edgett, K. S., & Castelltort, S. (2021). Global inventory of fluvial ridges on Earth and lessons applicable to Mars. *Earth-Science Reviews*, *216*, 103561. https://doi.org/10.1016/J.EARSCIREV.2021.103561

Zuber, M. T., Smith, D. E., Solomon, S. C., Muhleman, D. O., Head, J. W., Garvin, J. B., et al. (1992). The Mars observer laser altimeter investigation. *Journal of Geophysical Research*, *97*(E5), 7781–7797. https://doi.org/10.1029/92JE00341